

# Electrical tuning of valley magnetic moment through symmetry control in bilayer MoS<sub>2</sub>

Sanfeng Wu<sup>1</sup>, Jason S. Ross<sup>2</sup>, Gui-Bin Liu<sup>3</sup>, Grant Aivazian<sup>1</sup>, Aaron Jones<sup>1</sup>, Zaiyao Fei<sup>1</sup>, Wenguang Zhu<sup>4,5,6</sup>, Di Xiao<sup>5,7</sup>, Wang Yao<sup>3</sup>, David Cobden<sup>1</sup> and Xiaodong Xu<sup>1,2\*</sup>

**Crystal symmetry governs the nature of electronic Bloch states. For example, in the presence of time-reversal symmetry, the orbital magnetic moment and Berry curvature of the Bloch states must vanish unless inversion symmetry is broken<sup>1</sup>. In certain two-dimensional electron systems such as bilayer graphene, the intrinsic inversion symmetry can be broken simply by applying a perpendicular electric field<sup>2,3</sup>. In principle, this offers the possibility of switching on/off and continuously tuning the magnetic moment and Berry curvature near the Dirac valleys by reversible electrical control<sup>4,5</sup>. Here we investigate this possibility using polarization-resolved photoluminescence of bilayer MoS<sub>2</sub>, which has the same symmetry as bilayer graphene but has a bandgap in the visible spectrum<sup>6,7</sup> allowing direct optical probing<sup>5,8–12</sup>. We find that in bilayer MoS<sub>2</sub> the circularly polarized photoluminescence can be continuously tuned from –15% to 15% as a function of gate voltage, whereas in structurally non-centrosymmetric monolayer MoS<sub>2</sub> the photoluminescence polarization is gate independent. The observations are well explained as resulting from the continuous variation of orbital magnetic moments between positive and negative values through symmetry control.**

The Dirac-valley degree of freedom has recently been considered for new modes of electronic and photonic device operation<sup>4,5,9–17</sup> following the arrival of atomically thin two-dimensional (2D) electronic systems<sup>6,7,18,19</sup> (Fig. 1a). In this context, phenomena such as valley polarization and anomalous valley- and spin-Hall effects have been discussed for the +K and –K Dirac valleys at opposite corners of the Brillouin zone in hexagonal systems<sup>9–12,15</sup>. The realization of these effects hinges on achieving control of valley contrast, that is, of properties that differ between the two valleys, in particular the magnetic moment (**m**) and Berry curvature (**Ω**). Time-reversal symmetry dictates that each pseudovector, **m** as well as **Ω**, has the same magnitude but opposite sign in the two valleys, whereas inversion symmetry requires them to have the same sign. Therefore, a necessary condition for valley-contrasting **m** and **Ω** is inversion symmetry breaking<sup>4</sup>.

Monolayer MoS<sub>2</sub> lacks structural inversion symmetry (Fig. 1a), and thus **m** and **Ω** are non-zero, having equal magnitude but opposite signs in the two  $\pm K$  valleys owing to time-reversal symmetry. One direct consequence of non-zero **m** is valley-contrasting optical dichroism<sup>5,8,9</sup>, whereby charge carriers in the two valleys can be selectively excited by circularly polarized optical fields<sup>9–11</sup>. This effect permits optical generation of valley polarization, as recently demonstrated using polarized

photoluminescence measurements. However, continuous and reversible control of these valley-contrasting properties requires a system where the inversion symmetry can be controlled at will, which has not been achieved previously.

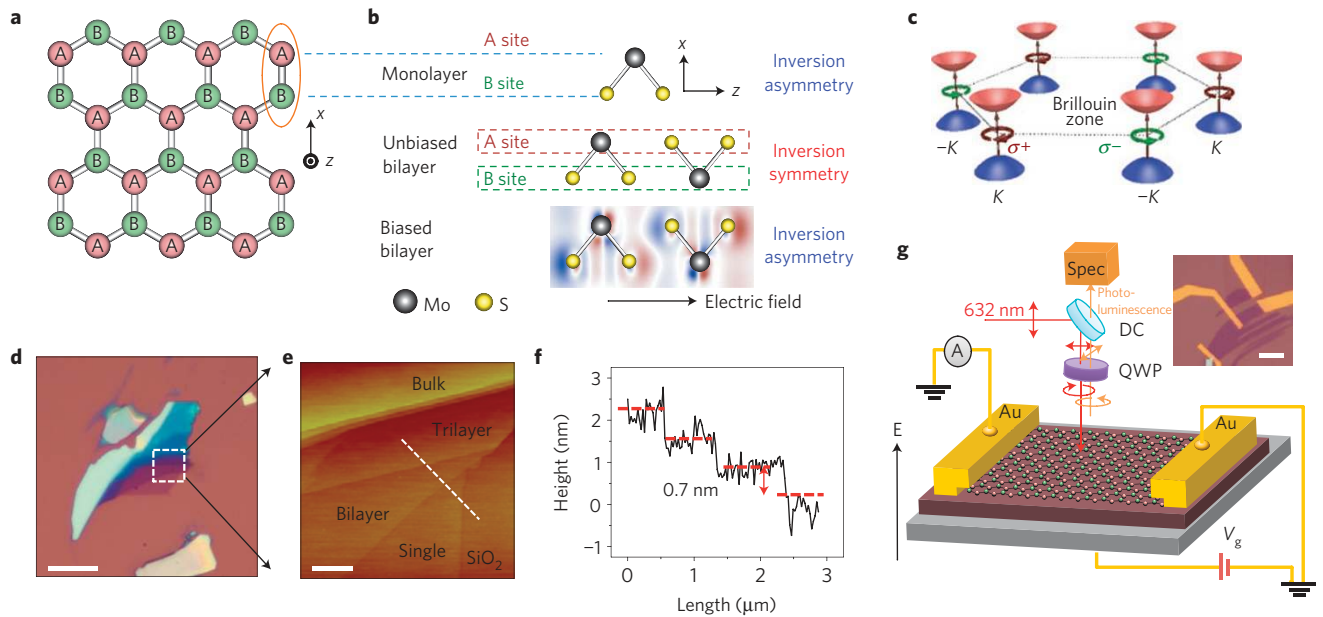
Unlike monolayer MoS<sub>2</sub> with its structural inversion asymmetry<sup>9,20,21</sup>, pristine bilayer MoS<sub>2</sub> is inversion symmetric (Fig. 1b)<sup>9,11,12</sup>. Thus, **m** and the consequent valley-contrasting dichroism vanish. However, inversion symmetry can be broken by applying an electric field perpendicular to the bilayer, which leads to a potential difference between the two layers (Fig. 1b, row 3). In bilayer graphene this perpendicular electric field produces a small bandgap<sup>2,3</sup>. In bilayer MoS<sub>2</sub>, which already has a bandgap in the visible<sup>6,7,19</sup>, the effect on the energy spectrum is negligible. This allows us to focus on the effect of the electric field on the orbital magnetic moments, which affect optical selection rules near the  $\pm K$  valleys<sup>9</sup> (Fig. 1c).

In our experiments, atomically thin MoS<sub>2</sub> samples are mechanically exfoliated from bulk MoS<sub>2</sub> crystals onto SiO<sub>2</sub> (285 nm thick) on heavily doped silicon<sup>18</sup>. Figure 1d is an optical micrograph of a representative sample. The number of layers is identified by atomic force microscopy, as illustrated in Fig. 1e,f, where the profile along the white dashed line clearly shows monolayer steps with a thickness<sup>7,17</sup> of about 7 Å. We then fabricate field-effect transistors (FETs) in which the back-gate voltage  $V_g$  controls the perpendicular electric field (Fig. 1g; refs 17,22–24 and Methods).

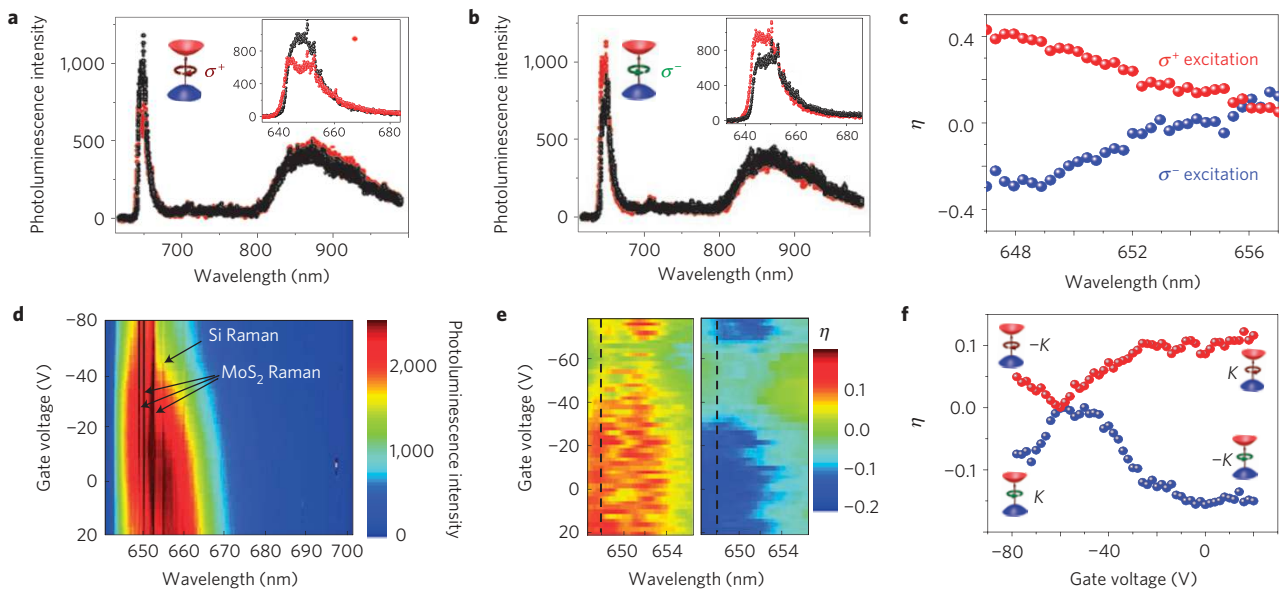
To perform polarization-resolved microphotoluminescence (see Methods for details), the excitation laser is incident normally on the sample, held at a temperature of 30 K, with a spot size of  $\sim 2 \mu\text{m}$ . The laser intensity is  $150 \text{ W cm}^{-2}$  and the wavelength is 632 nm unless otherwise noted. After interband excitation, for example by  $\sigma^+$  light, the right- and left-hand-polarized photoluminescence signals,  $P(\sigma^+)$  and  $P(\sigma^-)$ , are selectively detected. The degree of circular polarization is defined as  $\eta = (P(\sigma^+) - P(\sigma^-)) / (P(\sigma^+) + P(\sigma^-))$ . Note that all of the photoluminescence spectra presented here show a sharp drop below 645 nm due to the spectral cutoff of the laser notch filter.

Figure 2a,b shows the polarization-resolved photoluminescence spectra for bilayer MoS<sub>2</sub> on excitation by  $\sigma^+$  and  $\sigma^-$  polarized light, respectively, at  $V_g = 0$  for bilayer device B1. There are two spectral features. The broad peak centred on 860 nm shows no circular polarization, as expected for phonon-assisted indirect interband transitions. This peak is not the focus of the paper but it provides a convenient non-polarized reference signal. In contrast, the photoluminescence at 650 nm, which is from direct transitions

<sup>1</sup>Department of Physics, University of Washington, Seattle, Washington 98195, USA, <sup>2</sup>Department of Material Science and Engineering, University of Washington, Seattle, Washington 98195, USA, <sup>3</sup>Department of Physics and Center of Theoretical and Computational Physics, The University of Hong Kong, Hong Kong, China, <sup>4</sup>Department of Physics and Astronomy, University of Tennessee, Knoxville, Tennessee 37996, USA, <sup>5</sup>Materials Science and Technology Division, Oak Ridge National Laboratory, Oak Ridge, Tennessee 37831, USA, <sup>6</sup>ICQD/HFNL, University of Science and Technology of China, Hefei, Anhui 230026, China, <sup>7</sup>Department of Physics, Carnegie Mellon University, Pittsburgh, Pennsylvania 15213, USA. \*e-mail: xuxd@uw.edu.



**Figure 1 | MoS<sub>2</sub> devices and their symmetry properties.** **a**, Top view of the 2D hexagonal lattice structure. **b**, Side view of unit cells of the MoS<sub>2</sub> lattice structures. Top row: monolayer with structural inversion asymmetry. Middle row: pristine bilayer with inversion symmetry. Bottom row: change in electron density on application of a perpendicular electric field to the bilayer (DFT calculation), showing the absence of inversion symmetry. **c**, Schematic illustration of valley-contrasting circular dichroism when inversion symmetry is broken. **d**, Optical micrograph of a representative MoS<sub>2</sub> sample. Scale bar, 10  $\mu\text{m}$ . **e**, Atomic force micrograph of the area highlighted by the dashed square in **d**. Scale bar, 1  $\mu\text{m}$ . **f**, Line cut along the white dashed line in **e** showing the atomic layer thickness,  $\sim 0.7$  nm. **g**, Schematic of polarized photoluminescence measurements on a MoS<sub>2</sub> FET device (see Methods). Inset: optical micrograph of MoS<sub>2</sub> FET devices. QWP, quarter-wave plate; DC, dichroic beam splitter. Scale bar, 10  $\mu\text{m}$ .



**Figure 2 | Electrical control of valley magnetic moment in bilayer MoS<sub>2</sub> FETs.** **a, b**, Polarization-resolved photoluminescence excited by,  $\sigma^+$  (**a**) and  $\sigma^-$  (**b**) light at  $V_g = 0$ . Insets: zoomed-in photoluminescence spectra around 650 nm. Black (red):  $P(\sigma^+)$  ( $P(\sigma^-)$ ) signals. **c**, Degree of photoluminescence polarization as a function of wavelength. Red (blue):  $\sigma^+$  ( $\sigma^-$ ) excitation. **d**, Photoluminescence intensity map as a function of wavelength and gate voltage. **e**, Degree of photoluminescence polarization as a function of wavelength and gate voltage. The left (right) plot is obtained for  $\sigma^+$  ( $\sigma^-$ ) excitation. **f**, Degree of photoluminescence polarization as a function of gate voltage at 648 nm (line cuts along the dashed lines in **e**). Red (blue) dots denote  $\sigma^+$  ( $\sigma^-$ ) excitation.

in the  $\pm K$  valleys does show circular polarization. For  $\sigma^+$  excitation  $P(\sigma^+)$  is larger than  $P(\sigma^-)$  (Fig. 2a), and vice versa (Fig. 2b). The corrected polarization  $\eta$  is plotted against wavelength in Fig. 2c (see Methods). The increase in the magnitude of  $\eta$  towards shorter wavelength is characteristic of hot luminescence. The non-zero photoluminescence polarization at  $V_g = 0$  implies the existence of

broken inversion symmetry in the as-prepared bilayer, consistent with a recent report<sup>11</sup>. All of our bilayer devices showed  $\eta$  ranging from  $\sim 10$  to  $\sim 30\%$  at  $V_g = 0$  (Supplementary Information), with no clear dependence on laser intensity.

Figure 2d is a 2D intensity plot of  $P(\sigma^+)$  on  $\sigma^+$  excitation for bilayer device B2. The light emission is slightly blueshifted

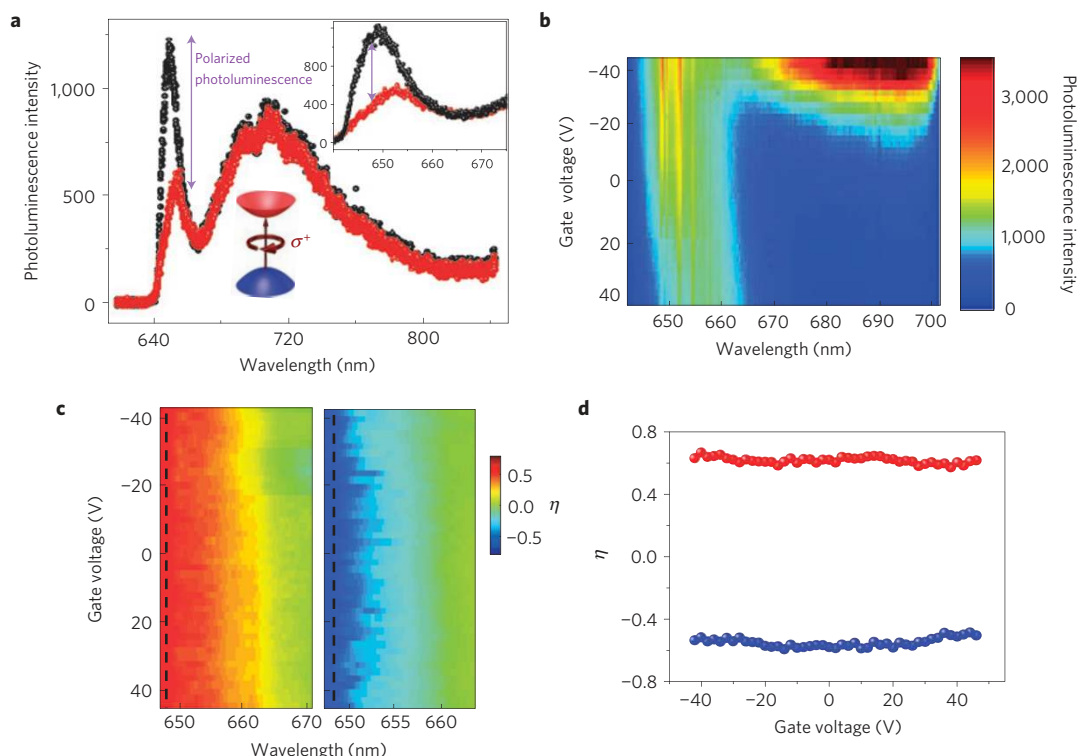


**Figure 3 | Gate-independent photoluminescence polarization of monolayer MoS<sub>2</sub> FETs.** **a**, Polarized photoluminescence at  $V_g = 0$  with  $\sigma^+$  excitation. Black (red):  $P(\sigma^+)$  ( $P(\sigma^-)$ ) signals. Insets: zoomed-in photoluminescence spectrum near 650 nm. **b**, Photoluminescence intensity map as a function of wavelength and gate voltage. **c**, Degree of photoluminescence polarization  $\eta$  as a function of wavelength and gate voltage. The left (right) plot is obtained for  $\sigma^+$  ( $\sigma^-$ ) excitation. **d**, Degree of photoluminescence polarization at 648 nm as a function of gate voltage (indicated by the dashed lines in **c**). Red (blue) dots represent photoluminescence polarization generated by  $\sigma^+$  ( $\sigma^-$ ) polarized light.

and its intensity decreases as  $V_g$  decreases from positive to negative (Supplementary Information). The sharp vertical lines superimposed on the photoluminescence are Raman scattering peaks<sup>25–27</sup>. Interestingly,  $\eta$  changes markedly as a function of  $V_g$ . Figure 2e is a colour map of  $\eta$  as a function of both wavelength and  $V_g$ . The data clearly show that  $\eta$  depends strongly on  $V_g$  and approaches zero around  $-60$  V. This observation implies that the sample is initially electron doped<sup>17</sup> (Supplementary Information).

The value of  $\eta$  at 648 nm (indicated by the dashed lines in Fig. 2e) is plotted against  $V_g$  in Fig. 2f for  $\sigma^+$  (red) and  $\sigma^-$  (blue) polarized light excitation. Together they form a striking X-shaped pattern. The photoluminescence polarization completely disappears at the centre of the X at  $V_c = -60$  V, and becomes finite on either increasing or decreasing  $V_g$  from there. Furthermore, the dependence of  $\eta$  on  $V_g$  is nonlinear: for  $|V_g - V_c| \gtrsim 30$  V it seems to approach saturation.

In sharp contrast, the spectra of monolayer MoS<sub>2</sub> devices (five were measured) exhibit no appreciable  $V_g$  dependence of  $\eta$ . Figure 3a illustrates photoluminescence spectra from monolayer device S1 under  $\sigma^+$  excitation at  $V_g = 0$ . The broad peak centred at 705 nm is probably from impurities. It does not show appreciable polarization and its intensity strongly depends on  $V_g$  (see Supplementary Information). In contrast, the narrower peak at 650 nm from transitions in the  $\pm K$  valleys is strongly polarized<sup>10–12</sup>. The polarization  $\eta$  reaches as much as 0.8 in some devices. Figure 3b shows a map of photoluminescence intensity versus  $V_g$  and wavelength for device S2. Again, the sharp vertical lines are Raman peaks that are superimposed on the photoluminescence of interest. The overall photoluminescence intensity has an appreciable dependence on  $V_g$ , but now  $\eta$  remains constant as  $V_g$  varies from  $-50$  to  $50$  V, as can be seen in the

map of  $\eta$  versus  $V_g$  and wavelength in Fig. 3c. Figure 3d shows  $\eta$  versus  $V_g$  at a wavelength of 648 nm for  $\sigma^+$  (red) and  $\sigma^-$  (blue) excitation, illustrating the markedly different behaviour from the bilayer case (Fig. 2f).

We now turn to the interpretation of these results. In the following discussion, all circular dichroism should be taken to be valley contrasting. Generally speaking, circularly polarized band-edge photoluminescence originates from optical selection rules, and the degree of photoluminescence polarization is determined by both the degree of circular dichroism and the depolarization mechanisms. Circular dichroism is related to the orbital magnetic moment as discussed in refs 5,8. In a hexagonal 2D crystal, for direct optical transitions at the  $\pm K$  valleys between a pair of bands labelled  $n$  and  $s$ , the  $k$ -resolved absorption circular dichroism is given by  $\chi(k) = (|P_+^{ns}(k)|^2 - |P_-^{ns}(k)|^2) / (|P_+^{ns}(k)|^2 + |P_-^{ns}(k)|^2)$ , where  $P_{\pm}^{ns}(k) = \langle u_s(k) | P_x \pm iP_y | u_n(k) \rangle$  is the interband matrix element of the momentum operator and  $|u_s(k)\rangle$  and  $|u_n(k)\rangle$  are the Bloch functions. The orbital magnetic moment is given by<sup>5</sup>  $\mathbf{m}_s(k) = (\hbar \mu_B / 2m_e) \sum_{n \neq s} (|P_+^{ns}(k)|^2 - |P_-^{ns}(k)|^2) / (\epsilon_n(k) - \epsilon_s(k))$ , where  $\mu_B$  is the Bohr magneton,  $m_e$  is free-electron mass,  $\epsilon_n(k)$  is the dispersion of the  $n$ th band, and  $\hat{z}$  is perpendicular to the sheet. It can be seen from the relationship between these expressions that  $\chi$  is finite when  $\mathbf{m}$  is finite.

It has been established that the polarized photoluminescence in monolayer MoS<sub>2</sub> originates from valley-contrasting circular dichroism<sup>9–11</sup>. Owing to absorption circular dichroism over a large range of  $k$  in each Dirac valley, circularly polarized light excites electrons preferentially in one valley producing valley polarization at the excitation energy. Because we detect photoluminescence from electrons that have relaxed to the band edge, the observed degree of photoluminescence polarization is determined by the absorption circular dichroism  $\chi$  at the excitation energy and the

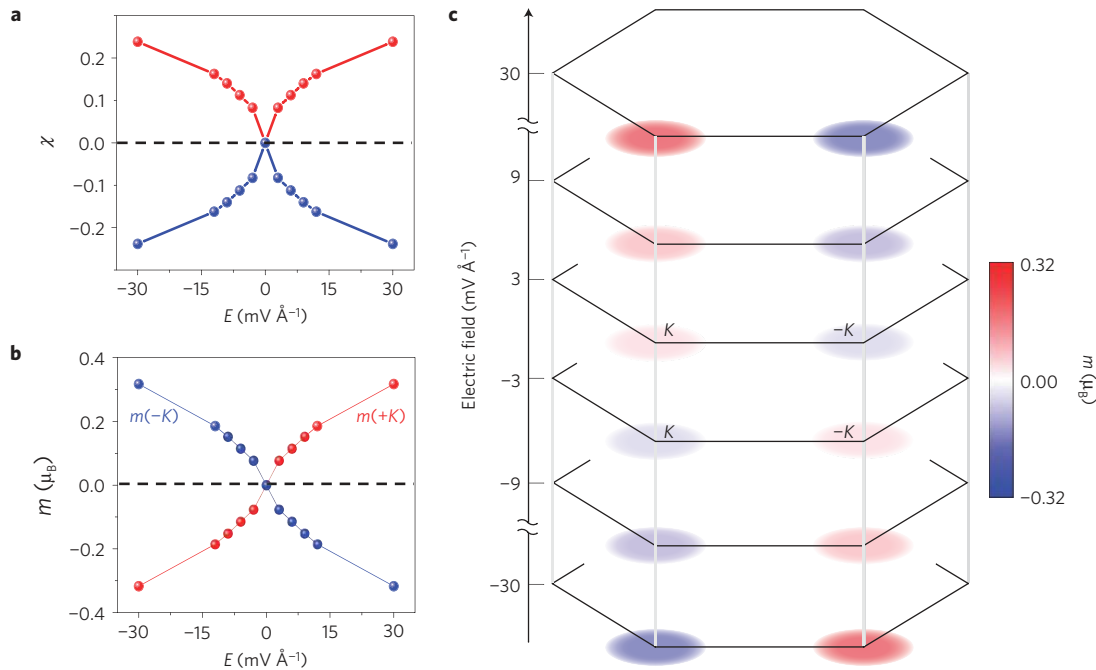


**Figure 4 | DFT calculation of magnetoelectric effect and associated circular dichroism.** **a**, Absorption circular dichroism  $\chi$  as a function of electric field. The positive (negative) value represents  $\sigma^+$  ( $\sigma^-$ ) excitation. **b**,  $\mathbf{m}$  at  $\pm K$  as a function of electric field, which shows that  $\mathbf{m}$  is an odd function of electric field. **c**, Colour map of  $\mathbf{m}$  as a function of electric fields near  $\pm K$  points in the momentum space.

valley depolarization rate (due to inter-valley scattering) during the hot-carrier relaxation. The large  $\eta$  observed here and in ref. 11 therefore implies not only large  $\chi$  in a large neighbourhood around the K points, but also that the valley relaxation time is longer than the electron-hole recombination time. The lack of dependence of  $\eta$  on  $V_g$  that we report here (Fig. 3d) demonstrates that the inter-valley scattering time remains long as the perpendicular electric field is changed. It also implies that both circular dichroism and  $\mathbf{m}$  are little affected by the electric field, consistent with the fact that in monolayer MoS<sub>2</sub> it is governed by the inherent structural inversion asymmetry.

The new X-shaped pattern of  $\eta$  versus  $V_g$  we observe in the bilayer case (Fig. 2f) can be explained well by the relation between inversion symmetry and orbital magnetic moment. When inversion symmetry is present in the bilayer at  $V_g = V_c$ ,  $\mathbf{m}$  and the associated valley-contrasting optical dichroism disappear. For all other values of  $V_g$ , inversion symmetry is broken and consequently non-zero  $\mathbf{m}$  and valley circular dichroism appear near the band edge, which leads to finite photoluminescence polarization. Thus, the observation of finite  $\eta$  signifies electric-field-induced  $\chi$  and  $\mathbf{m}$  with long valley relaxation time. The bilayer configurations at the two gate voltages  $V_g = V_c \pm \Delta V$  should be equivalent by spatial inversion, under which the  $+K$  and  $-K$  valley indexes are switched but the resulting photoluminescence polarization is unchanged. This is consistent with the pattern observed:  $\eta$  is always positive (negative) for  $\sigma^+$  ( $\sigma^-$ ) excitation and is symmetric with respect to  $V_c$ , as evident in Fig. 2f. Our results therefore demonstrate that inversion symmetry breaking by a perpendicular electric field can be used not only to modify the dispersion of the electron states, as has been shown in bilayer graphene, but also to control the orbital magnetic moments of Bloch states (see Supplementary Information for explicit relations between  $\mathbf{m}$  and  $\mathbf{\Omega}$  and the gate electric field derived in the  $k \cdot p$  approximation).

Although such an X-shaped pattern of  $\eta$  as a function of electric field has not been seen before, electric-field-dependent photoluminescence polarization is not unusual and has also been observed for example in GaAs quantum wells, where the

polarization is related to spin and the electric field affects the spin depolarization rate<sup>28</sup>. In our case, the observation of  $\eta = 0$  at  $V_g = V_c$  implies that spin relaxation is fast at the symmetry point, because the electrons remember none of the angular momentum of the absorbed light at that point. To explain the X-shaped pattern in terms of spin polarization one would have to assume that the spin relaxation rate decreases strongly with applied field away from the symmetry point. However, the spin relaxation rate is expected to be the smallest at the inversion symmetry point, for example a perpendicular electric field introduces Rashba spin-orbit coupling which normally increases the spin relaxation rate<sup>29</sup>. Furthermore, in the monolayer we observe a constant large photoluminescence polarization as a function of  $V_g$ , incompatible with a changing spin relaxation rate. Our observations are perfectly explained by slow inter-valley scattering leading to valley polarization at the band edge combined with fast spin relaxation and negligible spin polarization. Tuning of the relaxation rates is unlikely to be the cause of the observation.

As discussed above,  $\chi$  sets an upper bound on  $\eta$ . Therefore, we have performed *ab initio* density functional theory (DFT) calculations of both  $\chi$  and  $\mathbf{m}$  as a function of electric field in bilayer MoS<sub>2</sub>. Figure 4a shows the calculated  $\chi$  when the excitation energy is  $\sim 50$  meV above the DFT bandgap, roughly the energy difference between the incident photons and the photoluminescence peak position. The calculation reproduces the X-shaped pattern and qualitatively agrees with the experimental observation. Figure 4b,c shows the calculated orbital magnetic moment at  $\pm K$  valleys near the top valence band at various electric fields. We note that finite orbital magnetic moment also implies finite Berry curvature<sup>4,5,9,10</sup>, which also depends on the inter-band matrix element of the momentum operator and has a similar expression:  $\mathbf{\Omega}_s(\mathbf{k}) = -\hat{z}(1/2)(\hbar/m_e)^2 \sum_{n \neq s} (|P_{+}^{ns}(\mathbf{k})|^2 - |P_{-}^{ns}(\mathbf{k})|^2) / ((\epsilon_n(\mathbf{k}) - \epsilon_s(\mathbf{k}))^2)$ . Hence, the valley-contrasting magnetoelectric effect represents possible electrical control of the Berry curvature, suggesting the possibility of manipulating topological quantum phenomena in atomically thin 2D materials.



## Methods

**Device fabrication.** Devices were fabricated using standard electron beam lithography techniques, using an FEI Sirion scanning electron microscope with a Nabyt nanometre pattern generation system. An electron beam evaporator was then used to deposit 5 nm/50 nm of Ti/Au followed by a standard hot-acetone lift-off process.

**Polarization-resolved photoluminescence.** The polarization-resolved photoluminescence set-up is equipped with a high-power microscope (Olympus), a low-temperature microphotoluminescence cryostat (Janis) and a spectrometer with a CCD (charge-coupled device) detector. Figure 1g shows the measurement scheme. A linearly polarized laser beam, either horizontal or vertical, is reflected by a dichroic beam splitter and then passed through a quarter-wave plate. The circularly polarized light, either  $\sigma^+$  or  $\sigma^-$ , is focused by a  $\times 40$  objective lens onto the sample located in the cryostat. The photoluminescence signal is collected by the same lens and goes through the same quarter-wave plate. The  $\sigma^+$  ( $\sigma^-$ ) polarized photoluminescence is consequently converted to vertical (horizontal) linear polarization. The linearly polarized photoluminescence transmits through the dichroic beam splitter and is selectively detected with a linear polarizer. The measured photoluminescence polarization is corrected to compensate for the depolarization effects caused by the system, which mainly originate from the optics involved in the incident path and are determined by characterizing the beam polarization at the sample position. We also applied linearly polarized light to excite the device and confirmed that the resulting degree of polarization is zero.

Received 9 July 2012; accepted 4 December 2012; published online 27 January 2013

## References

- Xiao, D., Chang, M.-C. & Niu, Q. Berry phase effects on electronic properties. *Rev. Mod. Phys.* **82**, 1959–2007 (2010).
- Mak, K. F., Lui, C. H., Shan, J. & Heinz, T. F. Observation of an electric-field-induced band gap in bilayer graphene by infrared spectroscopy. *Phys. Rev. Lett.* **102**, 256405 (2009).
- Zhang, Y. *et al.* Direct observation of a widely tunable bandgap in bilayer graphene. *Nature* **459**, 820–823 (2009).
- Xiao, D., Yao, W. & Niu, Q. Valley-contrasting physics in graphene: Magnetic moment and topological transport. *Phys. Rev. Lett.* **99**, 236809 (2007).
- Yao, W., Xiao, D. & Niu, Q. Valley-dependent optoelectronics from inversion symmetry breaking. *Phys. Rev. B* **77**, 235406 (2008).
- Mak, K. F., Lee, C., Hone, J., Shan, J. & Heinz, T. F. Atomically thin MoS<sub>2</sub>: A new direct-gap semiconductor. *Phys. Rev. Lett.* **105**, 136805 (2010).
- Splendiani, A. *et al.* Emerging photoluminescence in monolayer MoS<sub>2</sub>. *Nano Lett.* **10**, 1271–1275 (2010).
- Souza, I. & Vanderbilt, D. Dichroic f-sum rule and the orbital magnetization of crystals. *Phys. Rev. B* **77**, 054438 (2008).
- Xiao, D., Liu, G.-B., Feng, W., Xu, X. & Yao, W. Coupled spin and valley physics in monolayers of MoS<sub>2</sub> and other group-VI dichalcogenides. *Phys. Rev. Lett.* **108**, 196802 (2012).
- Zeng, H., Dai, J., Yao, W., Xiao, D. & Xiaodong, C. Valley polarization in MoS<sub>2</sub> monolayers by optical pumping. *Nature Nanotech.* **7**, 490–493 (2012).
- Mak, K. F., He, K., Shan, J. & Heinz, T. F. Control of valley polarization in monolayer MoS<sub>2</sub> by optical helicity. *Nature Nanotech.* **7**, 494–498 (2012).
- Cao, T., Feng, J., Shi, J., Niu, Q. & Wang, E. Valley-selective circular dichroism of monolayer molybdenum disulphide. *Nature Commun.* **3**, 887 (2012).
- Akhmerov, A. R. & Beenakker, C. W. J. Detection of valley polarization in graphene by a superconducting contact. *Phys. Rev. Lett.* **98**, 157003 (2007).
- Rycerz, A., Tworzydło, J. & Beenakker, C. W. J. Valley filter and valley valve in graphene. *Nature Phys.* **3**, 172–175 (2007).
- Zhu, Z.-G. & Berakdar, J. Berry-curvature-mediated valley-Hall and charge-Hall effects in graphene via strain engineering. *Phys. Rev. B* **84**, 195460 (2011).
- Korn, T., Heydrich, S., Hirmer, M., Schmutzler, J. & Schuller, C. Low-temperature photocarrier dynamics in monolayer MoS<sub>2</sub>. *Appl. Phys. Lett.* **99**, 102109 (2011).
- Radisavljevic, B., Radenovic, A., Brivio, J., Giacometti, V. & Kis, A. Single-layer MoS<sub>2</sub> transistors. *Nature Nanotech.* **6**, 147–150 (2011).
- Novoselov, K. S. *et al.* Two-dimensional atomic crystals. *Proc. Natl Acad. Sci. USA* **102**, 10451–10453 (2005).
- Eda, G. *et al.* Photoluminescence from chemically exfoliated MoS<sub>2</sub>. *Nano Lett.* **11**, 5111–5116 (2011).
- Cheiwchanchamnangij, T. & Lambrecht, W. R. L. Quasiparticle band structure calculation of monolayer, bilayer, and bulk MoS<sub>2</sub>. *Phys. Rev. B* **85**, 205302 (2012).
- Zhu, Z. Y., Cheng, Y. C. & Schwingenschlög, U. Giant spin-orbit-induced spin splitting in two-dimensional transition-metal dichalcogenide semiconductors. *Phys. Rev. B* **84**, 153402 (2011).
- Yoon, Y., Ganapathi, K. & Salahuddin, S. How good can monolayer MoS<sub>2</sub> transistors be? *Nano Lett.* **11**, 3768–3773 (2011).
- Popov, I., Seifert, G. & Tománek, D. Designing electrical contacts to MoS<sub>2</sub> monolayers: A computational study. *Phys. Rev. Lett.* **108**, 156802 (2012).
- Radisavljevic, B., Whitwick, M. B. & Kis, A. Integrated circuits and logic operations based on single-layer MoS<sub>2</sub>. *ACS Nano* **5**, 9934–9938 (2011).
- Lee, C. *et al.* Anomalous lattice vibrations of single- and few-layer MoS<sub>2</sub>. *ACS Nano* **4**, 2695–2700 (2010).
- Jiménez Sandoval, S., Yang, D., Frindt, R. F. & Irwin, J. C. Raman study and lattice dynamics of single molecular layers of MoS<sub>2</sub>. *Phys. Rev. B* **44**, 3955 (1991).
- Chakraborty, B. *et al.* Symmetry-dependent phonon renormalization in monolayer MoS<sub>2</sub> transistor. *Phys. Rev. B* **85**, 161403 (2012).
- Balocchi, A. *et al.* Full electrical control of the electron spin relaxation in GaAs quantum wells. *Phys. Rev. Lett.* **107**, 136604 (2011).
- Koralek, J. D. *et al.* Emergence of the persistent spin helix in semiconductor quantum wells. *Nature* **458**, 610–614 (2009).

## Acknowledgements

The authors thank B. Spivak for helpful discussions. This work is mainly supported by the US DoE, BES, Division of Materials Sciences and Engineering (DE-SC0008145), and device fabrication is partially supported by the NSF (DMR-1150719). A.J. was supported by the NSF Graduate Research Fellowship (DGE-0718124). G.-B.L. and W.Y. were supported by the Research Grant Council of Hong Kong (HKU 706412P). W.Z. and D.X. were supported by US DoE, BES, Division of Materials Sciences and Engineering. D.C. and Z.F. were supported by the DoE BES (DE-SC0002197). The DFT calculations were performed at the National Energy Research Scientific Computing Center supported by the DoE Office of Science. Device fabrication was performed at the University of Washington Micro Fabrication Facility and NSF-funded Nanotech User Facility.

## Author contributions

All authors discussed the results and made critical contributions to the work.

## Additional information

Supplementary information is available in the [online version of the paper](#). Reprints and permissions information is available online at [www.nature.com/reprints](http://www.nature.com/reprints). Correspondence and requests for materials should be addressed to X.X.

## Competing financial interests

The authors declare no competing financial interests.